Inorganic Chemistry

Article

pubs.acs.org/IC

Synthesis and Theoretical Investigations of the Solid Solution $CeRu_{1-x}Ni_xAl$ (x = 0.1−0.95) Showing Cerium Valence Fluctuations

Oliver Niehaus,[†] Ute Ch. Rodewald,[‡] Paula M. Abdala,[§] Rachid St. Touzani,[⊥] Boniface P. T. Fokwa,[⊥] and Oliver Janka*[,‡]

[†]NRW Graduate School of Chemistry and [‡]Institut für Anorganische und Analytische Chemie, Westfälische Wilhelms-Universität Münster, Corrensstrasse 30, D-48149 Münster, Germany

[§]Swiss Norwegian Beamlines (SNBL) at the European Synchrotron Radiation Facility (ESRF), 6 Rue Jules Horowitz, BP 220, Grenoble, France

[⊥]Institut für Anorganische Chemie, RWTH Aachen, Landoltweg 1, D-52074 Aachen, Germany

Supporting Information

ABSTRACT: Members of the solid solution series of $CeRu_{1-x}Ni_xAl$ can be obtained directly by arc melting of the elements. The presented compounds with $0.1 \leq x \leq 0.85$ crystallize in the orthorhombic space group *Pnma* (No. 62) in the LaNiAl structure type, while for $0.9 \leq x \leq 1$, the hexagonal ZrNiAl-type structure is found. The orthorhombic members exhibit an anomaly in the trend of the lattice parameters as well as an interesting behavior of the magnetic susceptibility, suggesting that the cerium cations exhibit no local moment. Besides the mixed-valent nature of the cerium cations, valence fluctuations along with a change in the cerium oxidation state depending on the nickel content have been found. The oxidation state has been determined from the magnetic data and additionally by XANES. Density functional theory calculations have identified the shortest Ce−Ru interaction as decisive for the stability of the orthorhombic solid solution.

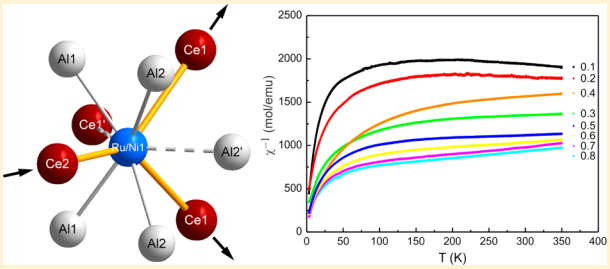

INTRODUCTION

The interest in intermetallic cerium compounds has increased steadily within the last 45 years because of their interesting physical properties. These properties are mainly based on the two possible valence states for cerium: the trivalent state with a [Xe] $4f^1$ electron configuration exhibiting paramagnetism and the tetravalent state with a [Xe] $4f^0$ electron configuration being diamagnetic. Interestingly, many of these cerium-containing compounds exhibit valence fluctuations and static or dynamic intermediate valence states. CeRuAl and CeNiAl are two members of the large group of *RETX* (*RE* = rare earth, *T* = transition metal, and *X* = main-group metal) compounds that exhibit these interesting properties.[1] Intermediate valence behavior is observed for CeRuAl with no magnetic ordering down to 2 K,[2,3] while for CeNiAl, also nonmagnetism[4] or mixed-valent magnetism[5] has been reported. Having somehow similar properties, CeNiAl and CeRuAl differ structurally: CeNiAl crystallizes in the hexagonal ZrNiAl-type structure [$P\bar{6}2m$ (No. 189)], while CeRuAl crystallizes in the orthorhombic LaNiAl-type structure [*Pnma* (No. 62)]. The ruthenium compound, furthermore, has unusually short Ce−Ru distances attributed to the $Ce^{(4-\delta)+}$ cations in the crystal structure.[3] For both CeNiAl[6] and CeRuAl,[3] theoretical calculations were conducted earlier. In the case of CeRuAl, the strong interactions between cerium and ruthenium are explained. Recently, the solid solution $CeNi_{0.5}Ru_{0.5}Al$ has been reported[7] which crystallizes in the orthorhombic CeRuAl structure and exhibits magnetic properties similar to those of the ternary phases for $T > 20$ K, but for $T < 20$ K, an abrupt increase in $\chi(T)$ is found near 10 K. Herein we report the full series of the solid solution $CeRu_{1-x}Ni_xAl$ with $0.1 \leq x \leq 0.95$ from the standpoint of structure and properties, combined with theoretical calculations in order to explain the features found.

RESULTS AND DISCUSSION

Crystal Structure. The crystal structures for the solid solutions of $CeRu_{1-x}Ni_xAl$ have been investigated from $0.1 \leq x \leq 0.95$ without the ternary end members CeRuAl and CeNiAl because they have been described in detail before. One major point of interest is the structural behavior regarding the point of structural change because the ternary compounds CeNiAl and CeRuAl crystallize in different structures. From $x = 0$ to 0.8, the members of the solid solutions crystallize in the orthorhombic LaNiAl-type structure with space group *Pnma*. The powder X-ray diffraction (XRD) pattern taken for $CeRu_{0.15}Ni_{0.85}Al$ from the as-cast button indicates the formation of both orthorhombic and hexagonal modifications. $CeRu_{0.1}Ni_{0.9}Al$ ($x = 0.9$) and $CeRu_{0.05}Ni_{0.95}Al$ ($x = 0.95$) finally crystallize in the hexagonal ZrNiAl-type structure [$P\bar{6}2m$ (No. 189), $Z = 3$]

Received: September 24, 2013
Published: February 14, 2014

   dx.doi.org/10.1021/ic402414f | *Inorg. Chem.* 2014, 53, 2471−2480

when characterized from powder XRD using the as-cast arc-melted button. After annealing at 850 °C, diffraction peaks of the orthorhombic modification of $CeNi_{0.1}Ru_{0.9}Al$ and $CeNi_{0.05}Ru_{0.95}Al$ arise in the powder XRD pattern, indicating that significant amounts of a second phase have formed. Energy-dispersive X-ray (EDX) analysis has shown that the two phases formed differ in their composition, with one being ruthenium-depleted and the other ruthenium-rich. The lattice parameters of the orthorhombic cell obtained from powder XRD for $0 \leq x \leq 0.85$ are plotted in Figure 1 (closed symbols and solid lines) along with the lattice parameters obtained from single-crystal diffraction (open symbols and dashed lines).

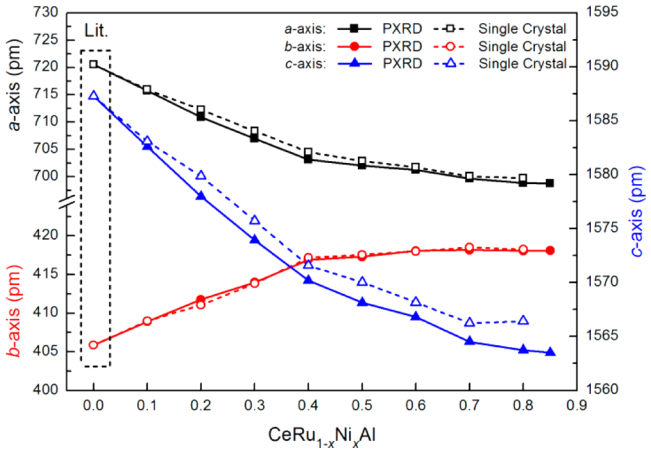

Figure 1. Lattice parameters of the orthorhombic members of $CeRu_{1-x}Ni_xAl$ versus the nickel content x.

The lattice parameters from both measurements are in good agreement, but they do not change linearly as expected. The lattice parameters exhibit a kink around $x = 0.4$ but show a linear trend between $x = 0$ and 0.4 and also between $x = 0.4$ and 0.8. From $x = 0.85$ to 1 (not shown here; see Table 1), the lattice parameters of the hexagonal representatives change linearly also. In order to understand this behavior of the cerium series in more detail, the solid solution for $LaRu_{1-x}Ni_xAl$ has been synthesized.

The lanthanum series has been synthesized from $x = 0.4-1$. For $x \leq 0.3$, the solid solution of $LaRu_{1-x}Ni_xAl$ does not form. The powder XRD data indicates the formation of LaNiAl along with RuAl. The lattice parameters of the stable members have been checked for an anomaly, but the a and c axes decrease linearly and the b axis increases linearly with increasing nickel content. Because no anomaly has been observed in the case of the lanthanum series, the kink of the cerium series has to be attributed to the special bonding situation between cerium and ruthenium (see the Theoretical Calculations section).

In the orthorhombic structures, cerium, aluminum, and the transition metal each occupy two distinct crystallographic sites. The two positions of the transition metal are mixed-occupied by ruthenium and nickel, comparable to what has been reported for $CeRu_{0.5}Ni_{0.5}Al$ before.[7] The crystal structure is described best by using the reduced coordination polyhedron surrounding the (Ru/Ni) sites in the shape of trigonal prisms of the compositions $[(Ru/Ni)1Ce_6]$ and $[(Ru/Ni)2Ce_2Al_4]$. The prisms are fused together over (Ce_2) edges to form branched, corrugated chains running along [100] that are further interlocked with chains of the other kind along the crystallographic c axis and a shift of $x/2$. They also alternate in height by $y/2$ (Figure 2, top). The structure can also be explained as an

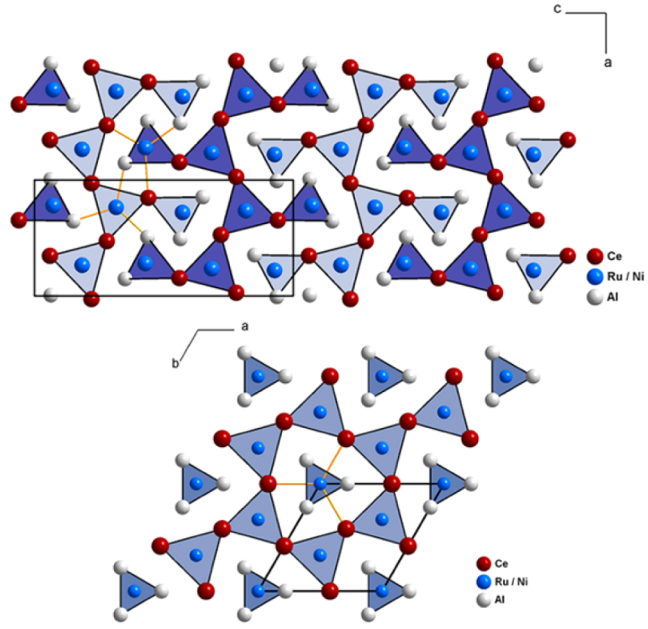

Figure 2. View of the extended unit cell of the orthorhombic (top) and hexagonal (bottom) structures of the solid solution $CeRu_{1-x}Ni_xAl$. The shifted chains in the case of the orthorhombic structure are highlighted by different colors (light blue at $y = 0$ and dark blue at $y = {}^1/_2$).

Table 1. Lattice Parameters from Powder XRD for $CeRu_{1-x}Ni_xAl$ ($x = 0.1-0.95$)

	x					
	0.1 (ortho.)	0.2 (ortho.)	0.3 (ortho.)	0.4 (ortho.)	0.5 (ortho.)	0.6 (ortho.)
a (pm)	715.77(5)	710.93(10)	707.01(9)	703.14(8)	702.05(9)	701.21(9)
b (pm)	408.92(5)	411.78(9)	414.01(5)	416.92(6)	417.29(6)	418.06(7)
c (pm)	1582.61(12)	1577.98(21)	1573.93(22)	1570.19(20)	1568.13(21)	1566.80(17)
V (Å^3)	463.22	461.95	460.70	460.31	459.40	459.30
	x					
	0.7 (ortho.)	0.8 (ortho.)	0.85 (ortho.)	0.85 (hex.)	0.9 (hex.)	0.95 (hex.)
a (pm)	699.68(8)	698.82(6)	698.75(5)	697.8(2)	697.60(8)	697.48(14)
b (pm)	418.18(9)	418.06(6)	418.10(4)			
c (pm)	1564.52(17)	1563.73(14)	1563.49(9)	402.3(1)	402.36(3)	402.39(6)
V (Å^3)	457.77	456.84	456.76	169.64	169.52	169.53

dx.doi.org/10.1021/ic402414f | Inorg. Chem. 2014, 53, 2471−2480

intergrowth of structural elements from the TiNiSi- and ZrNiAl-type structures (Figure 2, bottom).[8] The coordination polyhedra of the two mixed-occupied (Ru/Ni) positions exhibit a tricapped trigonal-prismatic coordination environment without any (Ru/Ni)−(Ru/Ni) contacts. For (Ru/Ni)1, the prism is formed by 2 × Ce and 4 × Al and by 2 × Ce and 1 × Al as capping atoms (Figure 3, left). The capping Ce2 atom exhibits

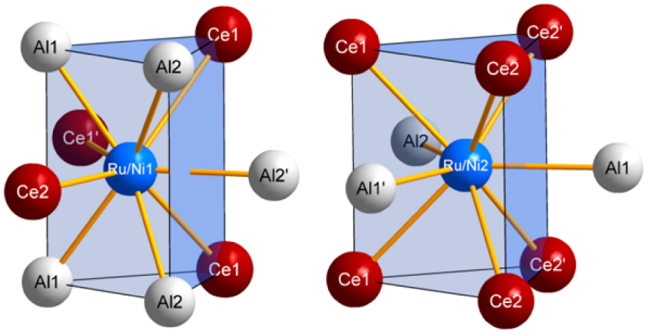

Figure 3. Tricapped trigonal prisms surrounding the mixed-occupied (Ru/Ni)1 (left) and (Ru/Ni)2 (right) positions.

an extremely short distance [d(Ce2−(Ru/Ni)1) = 267−280 pm], which is below the sum of the covalent radii (289 pm). Such short Ce−Ru distances can be found in a variety of intermetallic Ce*TX* compounds. The first compound reported with such short distances is CeRuSn.[9] Up to now, a large number of different compounds have been found; in all of them, this short distance is attributed to $Ce^{(4-\delta)+}$−Ru interactions.[3,10] For (Ru/Ni)2, the prism consists of 6 × Ce and 3 × Al atoms as capping atoms (Figure 3, right).

Taking a closer look at the interatomic distances in the (Ru/Ni) polyhedra, a feature similar to that of the kink in the lattice parameters is visible. The majority of the (Ru/Ni)−Al distances decrease linearly with increasing nickel content as expected; two of the capping aluminum atoms in the (Ru/Ni)2 polyhedra hardly change their distances (Figure 4). For the (Ru/Ni)−Ce distances, a linear change can be found for the capping cerium atoms, while the ones forming the direct coordination environment exhibit a kink at x = 0.4 (Figure 5). The shortest (Ru/Ni)1−Ce2 distance decreases rapidly (about 15 pm) with small changes in the nickel content, while the other two Ce1

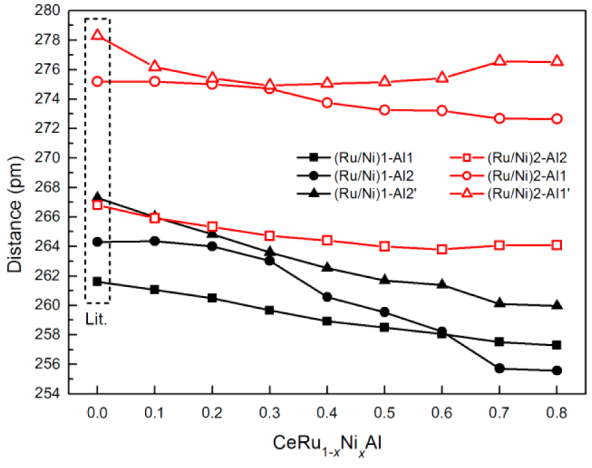

Figure 4. Interatomic distances d((Ru/Ni)−Al) in the orthorhombic members of $CeRu_{1-x}Ni_xAl$ versus the nickel content x.

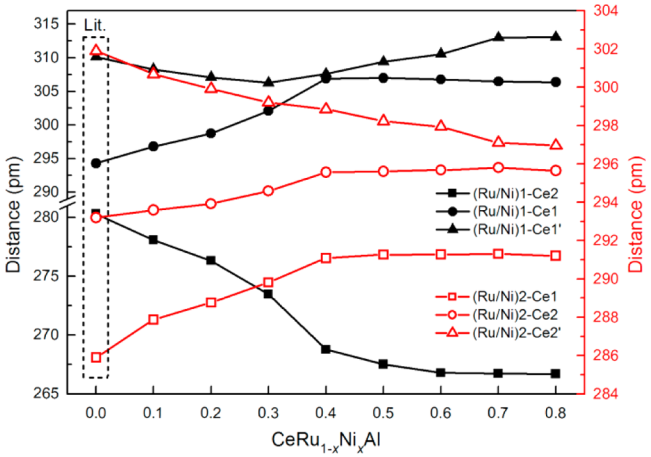

Figure 5. Interatomic distances d((Ru/Ni)−Ce) in the orthorhombic members of $CeRu_{1-x}Ni_xAl$ versus the nickel content x.

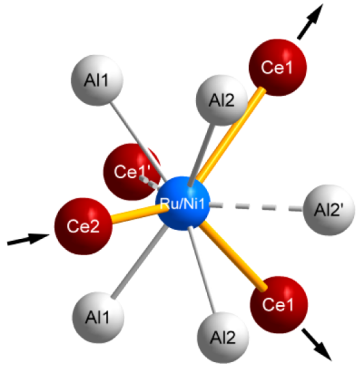

Figure 6. Illustration of the shrinking and expanding bonds in the (Ru/Ni)1 coordination environment.

distances elongate by about 5 pm each (Figure 6). The other (Ru/Ni)−Ce distances also elongate to compensate for the shrinking interatomic distance. All relevant details concerning the data collections are listed in Tables 2 and 3; Tables S1−S3 in the Supporting Information contain atomic coordinates and isotropic as well as anisotropic displacement parameters. Selected interatomic distances of orthorhombic $CeRu_{0.44(1)}Ni_{0.56(1)}Al$ and hexagonal $CeRu_{0.07(1)}Ni_{0.93(1)}Al$ are given in Table 4; a full list is given in Tables S4 and S5 in the Supporting Information.

Magnetic Properties. The inverse magnetic susceptibility data for the orthorhombic representatives of $CeRu_{1-x}Ni_xAl$ ($0.1 \leq x \leq 0.8$) measured with an applied field of H = 10 kOe are summarized in Figure 7. The susceptibility of all compounds is small (on the order of 10^{-3} emu mol^{-1}) without any magnetic ordering down to low temperatures as described in the case of CeNiAl.[4] Especially, the susceptibitlity curves of the compounds with $x < 0.3$ turn down for $T > 150$ K. Consequently, no Curie−Weiss behavior is observed. Although one might interpret the shape of the curves of $x > 0.3$ as linear, no Curie−Weiss fitting is applicable. The low-temperature behavior of all compounds can be attributed to Ce^{3+} impurities, while the shape of the χ^{-1} curves with the weak temperature dependence is typical for cerium-based intermetallics, which exhibit valence fluctuations. The magnetic susceptibility of valence-fluctuating compounds can be described with the interconfiguration fluctuation (ICF) model proposed by Hirst[11] and later applied by Sales and Wohlleben in order to explain the valence-

dx.doi.org/10.1021/ic402414f | Inorg. Chem. 2014, 53, 2471−2480

Table 2. Crystallographic Data and Details of the Single-Crystal Structure Refinements for $CeRu_{1-x}Ni_xAl$ (x = 0.1−0.5)

refined formula	$CeRu_{0.86(1)}Ni_{0.14(1)}Al$	$CeRu_{0.80(1)}Ni_{0.20(1)}Al$	$CeRu_{0.70(1)}Ni_{0.30(1)}Al$	$CeRu_{0.51(1)}Ni_{0.49(1)}Al$	$CeRu_{0.44(1)}Ni_{0.56(1)}Al$
depository no.	426680	426679	426687	426686	426685
temperature	room temperature	room temperature	room temperature	room temperature	room temperature
cryst syst	orthorhombic	orthorhombic	orthorhombic	orthorhombic	orthorhombic
space group	*Pnma* (No. 62)	*Pnma* (No. 62)	*Pnma* (No. 62)	*Pnma* (No. 62)	*Pnma* (No. 62)
cryst size (μm^3)	20 × 20 × 120	10 × 20 × 100	40 × 40 × 60	20 × 20 × 120	30 × 30 × 100
lattice param					
a (pm)	715.96(4)	712.31(4)	708.35(3)	704.52(2)	702.88(2)
b (pm)	409.00(2)	411.06(2)	413.84(2)	417.19(1)	417.57(1)
c (pm)	1583.09(6)	1579.87(8)	1575.71(8)	1571.58(6)	1570.04(4)
volume V ($Å^3$)	463.57	462.59	461.91	461.92	460.81
formula units (Z)	8	8	8	8	8
calcd densityD_x (g/cm^3)	7.52	7.46	7.34	7.12	7.05
diffractometer	Stoe IPDS II	Stoe IPDS II	Stoe IPDS II	Stoe IPDS II	Stoe IPDS II
radiation	Mo Kα	Mo Kα	Mo Kα	Mo Kα	Mo Kα
wavelength λ (pm)	71.073	71.073	71.073	71.073	71.073
$\pm h_{max}/\pm k_{max}/\pm l_{max}$	11/−6, +5/25	11/6/25	11/−6, +5/25	11/6/25	10/−6, +5/23
$\theta_{min}/\theta_{max}$ (deg)	3.12/34.88	2.58/34.83	3.15/34.84	3.17/34.91	2.59/31.88
$F(000)$	903	894	881	858	849
abs coeff μ (mm^{-1})	26.0	26.2	26.4	26.7	26.9
data correction	background, polarization and Lorentz factors, numerical absorption correction				
reflns, unique	26472, 1126	13505, 1123	13357, 1117	27233, 1123	19720, 886
R_{int}/R_σ	5.56/2.43	4.28/2.52	5.40/2.65	3.96/0.97	4.58/1.09
reflns with $\lvert F_o\rvert \geq 4\sigma(F_o)$	921	934	926	1027	857
structure determination and refinement	programs *SHELXS-97* and *SHELXL-97*[29]				
scattering factors	*International Tables*, Vol. C[30]				
R1/R1 with $\lvert F_o\rvert \geq 4\sigma(F_o)$	2.23/1.25	2.16/1.34	3.66/2.65	2.10/1.68	2.02/1.88
wR2/GOF	1.64/0.793	1.75/0.806	5.21/1.104	3.69/1.161	3.94/1.072
extinction (g)	0.0009(1)	0.0013(1)	0.0014(1)	0.0034(2)	0.0016(1)
residual electron density ρ ($e^- \times 10^6$ pm^{-3})					
max	1.06	0.84	1.29	1.30	0.94
min	−0.98	−1.11	−1.75	−1.98	−1.22

Further details of the crystal structure investigations can be obtained from the Fachinformationszentrum (FIZ) Karlsruhe, 76344 Eggenstein-Leopoldshafen, Germany (fax +49-7247-808-666; e-mail crysdata@fiz-karlsruhe.de), upon quoting the depository no. given above.

fluctuation behavior observed in intermetallic ytterbium compounds.[12] The ICF model can be used for systems where two distinct states of the rare-earth atom, here Ce^{3+}/Ce^{4+}, exist.

The temperature dependence of the magnetic susceptibility is described as

$$\chi(T) = \left(\frac{N_A}{3k_B}\right)\left[\frac{\mu_n^2 \nu(T) + \mu_{n-1}^2\{1-\nu(T)\}}{T + T_{sf}}\right] + n\frac{C}{T} + \chi_0 \quad (1)$$

with N_A being Avogardo's number, k_B Boltzmann's constant, μ the magnetic moment of the respective cerium ion, and T_{sf} the spin-fluctuation temperature. χ_0 is a temperature-independent term, C the Curie constant (for free Ce^{3+}, C = 0.807 emu mol^{-1} K^{-1}), and n the fraction of stable Ce^{3+}. The overall susceptibility is described by three terms: (i) a valence fluctuation part; (ii) the contribution of the stable Ce^{3+} ions; (iii) a temperature-independent part. The valence fluctuations are described by the pseudo-Boltzmann statistic shown in eq 2, which contains the spin-fluctuation temperature T_{sf} and E_{ex}, which describes the energy difference between the two cerium ground states according to $E_{ex} = E(Ce^{3+}) - E(Ce^{4+})$.

$$\nu(T) = \frac{2J_n + 1}{(2J_n + 1) + (2J_{n-1} + 1)\exp[E_{ex}/k_B(T + T_{sf})]} \quad (2)$$

For the cerium cations, the fluctuations take place between the $4f^0$ and $4f^1$ configurations. With $J_1 = \mu_1 = 0$, $J_2 = {}^5/_2$, and μ_{eff} = 2.54 μ_B, the magnetic data can be fitted and T_{sf}, E_{ex}, n, and χ_0 can be extracted. In order to prevent overdetermination, the temperature-independent part χ_0 and n were fitted first and fixed for the rest of the procedure. Table 5 contains the parameters determined from the respective measurements.

In addition to parameters extracted from the fitted data, the average cerium valence can be obtained using eq 2 to calculate $\nu(T)$. The change of the cerium valence versus temperature is plotted in Figure 8. Here two phenomena are clearly visible. First, a temperature-dependent shift of the cerium valence is visible. For all samples, a decrease is observed when going to higher temperatures, which is consistent with the valence fluctuations postulated earlier.[13] Second, the cerium valence seems to form sections. For x = 0.1−0.3, a cerium valence of +3.41 can be found at 350 K. For x = 0.4−0.5, the valence drops to about +3.31, and finally for x = 0.6−0.8, the cerium valence decreases to +3.25 (Figure 9). This behavior can be attributed to substitution of the "electron-poor" ruthenium by the more "electron-rich" nickel atoms. The additional electrons introduced, therefore, change the valence electron concentration (VEC) and shift the cerium valence more toward a trivalent state.

X-ray Absorption Near-Edge Structure (XANES). XANES at the Ce L_{III}-edge has been widely used for detecting

dx.doi.org/10.1021/ic402414f | Inorg. Chem. 2014, 53, 2471−2480

Table 3. Crystallographic Data and Details of the Single-Crystal Structure Refinements for $CeRu_{1-x}Ni_xAl$ (x = 0.6−0.9)

empirical formula	$CeRu_{0.38(1)}Ni_{0.62(1)}Al$	$CeRu_{0.20(1)}Ni_{0.80(1)}Al$	$CeRu_{0.20(1)}Ni_{0.80(1)}Al$	$CeRu_{0.07(1)}Ni_{0.93(1)}Al$
depository number	426684	426683	426682	426681
temperature	room temperature	room temperature	room temperature	room temperature
cryst syst	orthorhombic	orthorhombic	orthorhombic	hexagonal
space group	*Pnma* (No. 62)	*Pnma* (No. 62)	*Pnma* (No. 62)	$P\bar{6}2m$ (No. 189)
cryst size (μm^3)	20 × 20 × 80	10 × 20 × 100	20 × 20 × 100	20 × 40 × 100
lattice param				
a (pm)	701.74(5)	700.06(5)	699.73(3)	698.05(3)
b (pm)	418.00(2)	418.54(2)	418.26(2)	
c (pm)	1568.16(8)	1566.24(10)	1566.42(7)	402.31(2)
volume V ($Å^3$)	459.98	458.91	458.44	169.77
formula units (Z)	8	8	8	3
calcd density D_x (g/cm^3)	6.98	6.79	6.79	6.71
diffractometer	Stoe IPDS II	Stoe IPDS II	Stoe IPDS II	Stoe IPDS II
radiation	Mo Kα	Mo Kα	Mo Kα	Mo Kα
wavelength λ (pm)	71.073	71.073	71.073	71.073
$\pm h_{max}/\pm k_{max}/\pm l_{max}$	11/−6, +5/25	11/6/25	11/6/−24, 25	11/11/6
$\theta_{min}/\theta_{max}$ (deg)	3.18/34.94	3.19/34.83	2.60/34.85	3.37/34.81
$F(000)$	840	818	818	143
abs coeff μ (mm^{-1})	27.0	27.4	27.4	28.0
data correction	background, polarization and Lorentz factors, numerical absorption correction			
reflns, unique	31685, 1122	13757, 1113	15866, 1113	8694, 310
R_{int}/R_σ	11.21/5.18	9.72/6.87	4.91/2.31	3.93/0.91
reflns with $\lvert F_o\rvert \geq 4\sigma(F_o)$	787	726	923	300
structure determination and refinement	programs *SHELXS-97* and *SHELXL-97*[29]			
scattering factors	*International Tables*, Vol. C[30]			
R1/R1 with $\lvert F_o\rvert \geq 4\sigma(F_o)$	4.67/2.36	4.86/2.01	2.10/1.26	1.21/1.21
wR2/GOF	3.58/0.853	2.19/0.658	1.94/0.887	3.05/1.275
extinction (g)	0.0016(1)	0.0007(1)	0.0021(1)	0.0257(16)
residual electron density ρ ($e^- \times 10^6$ pm^{-3})				
max	1.77	1.08	0.92	1.04
min	−2.42	−1.55	−0.88	−0.73

Further details of the crystal structure investigations can be obtained from the Fachinformationszentrum (FIZ) Karlsruhe, 76344 Eggenstein-Leopoldshafen, Germany (fax +49-7247-808-666; e-mail crysdata@fiz-karlsruhe.de), upon quoting the depository no. given above.

Table 4. Interatomic Distances of Two Selected Representatives: Orthorhombic $CeRu_{0.44(1)}Ni_{0.56(1)}Al$ and Hexagonal $CeRu_{0.07(1)}Ni_{0.93(1)}Al$

Ce1−	Ru/Ni2	2	291.26(5)	Ce2−	Ru/Ni1	1	267.52(7)	Ru/Ni1−	Al1	2	258.49(11)
	Ru/Ni1	2	306.97(7)		Ru/Ni2	2	295.61(5)		Al2	2	259.54(18)
	Ru/Ni1	1	309.37(5)		Ru/Ni2	2	298.23(5)		Al2	1	261.69(11)
	Al2	1	314.81(17)		Al1	2	316.97(13)		Ce1	1	306.97(7)
	Al2	2	317.86(13)		Al2	2	324.52(13)		Ce1	2	309.36(5)
	Al1	2	329.34(17)		Al1	2	328.40(14)				
	Al1	1	329.62(14)								
Ru/Ni2−	Al2	1	264.00(18)	Al1−	Ru/Ni1	2	258.49(11)	Al2−	Ru/Ni1	2	261.69(11)
	Al1	1	273.26(18)		Ru/Ni2	1	275.15(19)		Al2	2	285.2(3)
	Al1	1	275.15(19)		Al2	1	285.2(3)		Al1	1	287.4(2)
	Ce1	2	291.26(5)		Ce2	2	316.97(13)		Ce1	1	314.81(17)
	Ce2	2	295.61(5)		Ce2	1	328.39(14)				
	Ce2	2	298.23(5)								
Ce1−	Ru/Ni1	4	289.96(1)	Ru/Ni1−	Al1	3	275.5(2)	Al1−	Ni2	2	257.7(2)
	Ni2	1	294.17(4)		Ce1	6	289.96(1)		Ru/Ni1	2	275.5(2)
	Al1	2	315.3(2)						Al1	2	279.0(4)
	Al1	1	324.90(3)	Ni2−	Al1	6	257.7(2)		Ce1	2	315.3(2)
					Ce1	3	294.17(4)		Ce1	4	324.90(3)

mixed valence in several cerium-based materials. It provides a representation of the electronic configuration and yields the 4f occupation number. The energies of the Ce $4f^0$ and $4f^1$ configurations are both located close to each other in the ground state of the mixed-valence compounds and show mixing due to the hybridization between the 4f and conduction band states. In the final state of the Ce L_{III} X-ray absorption spectrum, the energies of the two electronic configurations are assumed to be separated by a strong core−hole potential (10 eV) on the 4f state. Therefore, the spectra of mixed-valence

dx.doi.org/10.1021/ic402414f | Inorg. Chem. 2014, 53, 2471−2480

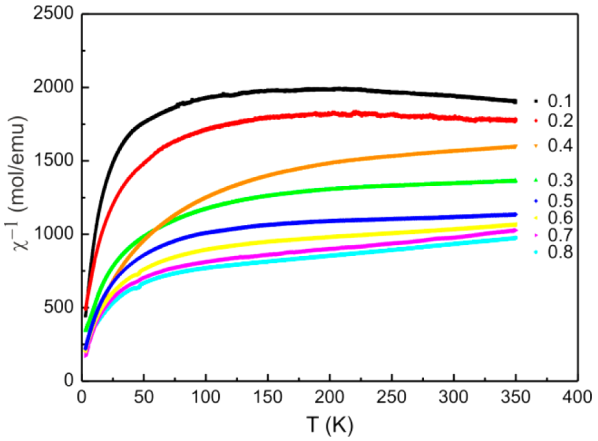

Figure 7. Inverse magnetic susceptibility data of $CeRu_{1-x}Ni_xAl$ for different nickel contents x plotted versus the temperature.

Table 5. Parameters of the Sales and Wohlleben Model Extracted from the Fit of the Inverse Susceptibility Data for $CeRu_{1-x}Ni_xAl$

x	E_{ex}/k_B (K)	T_{sf} (K)	n	χ_0 (emu mol^{-1})	valence at 350 K
0.1	2955(3)	1752(3)	0.0076	3.8×10^{-4}	3.41
0.2	3027(7)	1888(7)	0.0105	4.0×10^{-4}	3.39
0.3	3508(10)	2008(7)	0.0041	5.6×10^{-4}	3.42
0.4	2117(1)	1859(2)	0.0295	3.5×10^{-4}	3.30
0.5	2077(1)	1665(8)	0.0200	6.3×10^{-4}	3.32
0.6	805(9)	939(29)	0.0202	4.7×10^{-4}	3.24
0.7	525(1)	471(3)	0.0196	2.7×10^{-4}	3.24
0.8	507(1)	446(3)	0.0208	2.9×10^{-4}	3.24

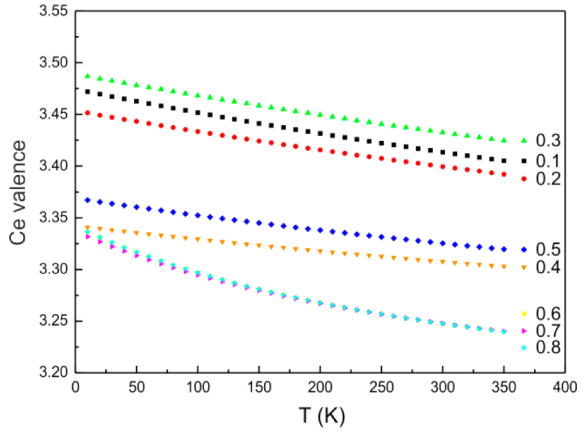

Figure 8. Cerium valence calculated from the fitted susceptibility data for different nickel contents x plotted versus the temperature for $CeRu_{1-x}Ni_xAl$.

compounds exhibit the characteristic double-peak profile. When it is assumed that the L_{III} absorption is a single-particle process and final state effects are neglected, the intensity ratio of the two peaks can be used for an estimation of the averaged valence number as applied in a wide variety of mixed-valence rare-earth-based materials before.[14−21]

The normalized Ce L_{III}-edge XANES spectrum for $CeRu_{0.5}Ni_{0.5}Al$ is presented in Figure 10. It shows a main "white line" at an energy of 5724 eV, which can be attributed to the final state configuration of Ce^{3+}, and a shoulder at an energy of nearly 9.3 eV above the main white line representing Ce^{4+}.

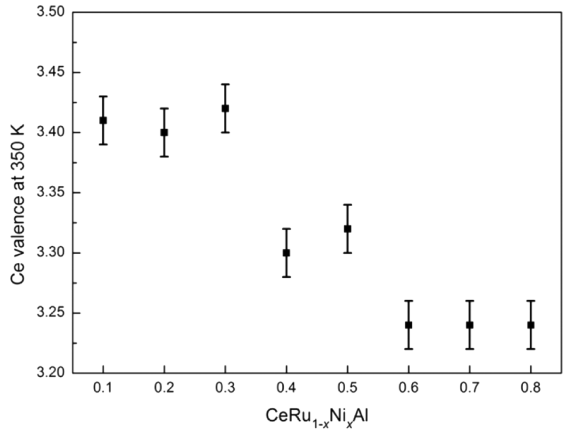

Figure 9. Calculated cerium valence at 350 K plotted versus the different nickel contents x for $CeRu_{1-x}Ni_xAl$.

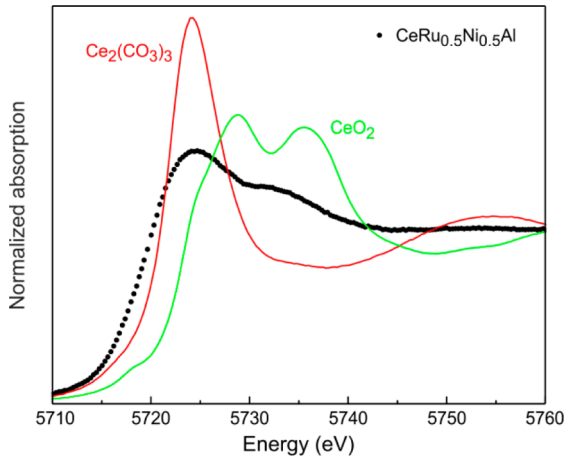

Figure 10. Normalized Ce L_{III} XANES spectra of $CeRu_{0.5}Ni_{0.5}Al$ plotted together with the reference substances $Ce_2(CO_3)_3$ and CeO_2.

The shape of the XANES profile qualitatively confirms the presence of the cerium mixed-valence state. In order to obtain the average valence number, the spectrum was fitted using a simplified model that consists of two arctangent functions describing the transitions to the continuum states and two Lorentzian functions taking into account the 4f states. Because of the high overlap of these functions, the fittings were performed by carefully varying the parameters that define the Lorentzian and arctangent functions (see Figure S2 in the Supporting Information). The energy gap between the two components was determined to be 9.2 eV for $CeRu_{0.5}Ni_{0.5}Al$. The ratio of the fractions of Ce^{4+} and Ce^{3+} ions was estimated by the ratio of the areas of the two Lorentzian curves to be 3.15. This value is significantly smaller than the one obtained by susceptibility measurements (3.32). Taking into account that the cerium valence in CeO_2 determined by XANES is only about 3.5, the results of both methods are consistent.[22]

Theoretical Calculations. Of all (Ru/Ni)−Ce distances experimentally found in the $CeRu_{1-x}Ni_xAl$ solid solution, one [d(Ru/Ni)1−Ce2] is decisively smaller (d < 280 pm) than the rest and even decreases further to 267 pm at x = 0.5 and then remains constant until x = 0.85. The aim of this section is, first, to study the influence of ruthenium substitution by nickel on this short distance and, second, to try to understand why the maximal amount of nickel cannot exceed x = 0.85. For these purposes, we have carried out electronic structure calculations

dx.doi.org/10.1021/ic402414f | Inorg. Chem. 2014, 53, 2471−2480

and bonding analyses based on the following structures: experimental $CeRu_{1-x}Ni_xAl$ (x = 0 and 0.5, LaNiAl-type), hypothetical $CeRu_{1-x}Ni_xAl$ (x = 1, using the experimental lattice parameters of x = 0.5), and experimental CeNiAl (hexagonal ZrNiAl-type structure). In order to take into account the 50% (Ru/Ni) mixed occupation in the x = 0.5 composition, a translationengleiche subgroup [$P2_1/m$ (No. 11), with $\beta = 90°$] of space group *Pnma* was used. In space group $P2_1/m$, all positions are doubled, thus enabling the positioning of nickel and ruthenium on distinct sites and therefore also the construction of six different models due to permutation of the nickel and ruthenium positions (see Tables S6 and S7 in the Supporting Information).

Our density-of-states (DOS) results for the experimentally found ternary phases corroborate very well with that of Miller et al. (for CeNiAl, the ZrNiAl type)[6] and that of Pöttgen et al. (for CeRuAl, the LaNiAl type).[3] The DOS curve of the hypothetical CeNiAl (the LaNiAl type, calculated using the lattice parameters of the x = 0.5 phase) is qualitatively similar to that of the experimental hexagonal phase (see Figure 11, left

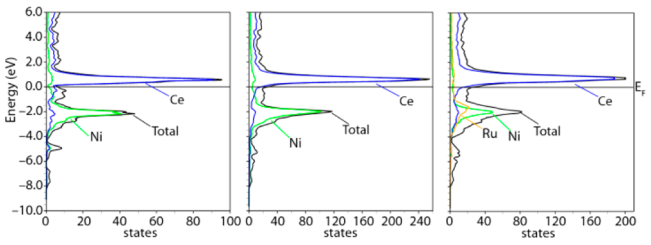

Figure 11. DOS of CeNiAl (left) in the experimental hexagonal ZrNiAl-type structure and (middle) in the hypothetical orthorhombic LaNiAl-type structure (with lattice parameters of $CeRu_{1-x}Ni_xAl$, x = 0.5) and (right) DOS of $CeRu_{1-x}Ni_xAl$, x = 0.5 (the LaNiAl type) in model E.

and middle), both having a deep pseudogap around the Fermi level. However, a small difference in the positioning of the Fermi level of the two phases exists: while E_F for the experimental hexagonal phase coincides with the minimum of the pseudogap, E_F of the hypothetical phase lies just above it. Although this may not be interpreted as a sign of instability of the orthorhombic structure, it hints at the preference of CeNiAl for the hexagonal structure, as found experimentally. A similar observation can be made on the −COHP curves of the Ce−Ni interaction in the two structures (see Figure 12, left and middle). This interaction is not optimized in the two structures because bonding states are found at and above E_F; however, at

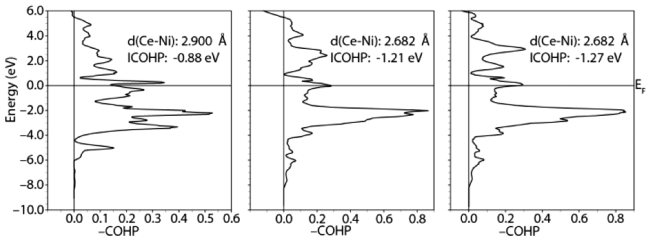

Figure 12. −COHP plot of the shortest Ce−Ni interaction (left) in the experimental hexagonal ZrNiAl-type structure, (middle) in the hypothetical orthorhombic LaNiAl-type structure (with lattice parameters of $CeRu_{1-x}Ni_xAl$, x = 0.5), and (right) in $CeRu_{1-x}Ni_xAl$, x = 0.5 (the LaNiAl type) in model E.

E_F, the Ce−Ni interaction of the hexagonal structure lies at a minimum, whereas in the orthorhombic structure, E_F passes through a maximum, although the Ce−Ni distance is shorter in the latter case. These findings indicate that the CeNiAl phase indeed prefers the LaNiAl type over the ZrNiAl type, as found experimentally. Nevertheless, the overall electronic behavior of CeNiAl in the orthorhombic structure indicates that a different synthetic strategy may still lead to its preparation.

Now we want to focus on the solid solution $CeRu_{1-x}Ni_xAl$ and explain why the maximal amount of nickel cannot exceed x = 0.8 by targeting the short Ce−T (T = Ni or Ru) bond, which becomes constant at x = 0.5 and above. As already mentioned, we have used for these calculations the $CeRu_{1-x}Ni_xAl$ (x = 0.5) composition and different structural models (see Table S7 in the Supporting Information). The main advantage of these models is that nickel is allowed to build the short Ce−T (T = Ni or Ru) distances (model C), share them with ruthenium (models D−G), or does not participate at all (model B). All DOS from these structural models are qualitatively similar to that of model E (see Figure 11, right). Furthermore, no significant difference can be found between these DOS. The chemical bonding around Ce2, however, depends on the positions of nickel and ruthenium around Ce2. First, the −COHP curves of the short Ce−Ni bond, in all models containing this bond, are similar in shape to those of model A, but their Fermi levels have significantly shifted from the maximum (see model A, Figure 12, middle) to near the pseudogap (see model E, Figure 12, right), indicating stabilization of this bond when ruthenium is present in the structure, as found experimentally. This is also confirmed by its ICOHP value, which is always smaller in the ternary than in the quaternary (see Table 6). In the following, we will examine the influence of the Ni/Ru permutations around Ce2 by comparing the ICOHP values of the same Ce−T (T = Ni or Ru) bonds around Ce2. For symmetry reasons, some models are identical (D and F, E and G); thus, the following comparisons are possible: B vs D vs E (all have at least one short Ce−Ru bond) and C vs D vs E (all have at least one short Ce−Ni bond). We have two ways to do this comparison.

In the first method, a simple addition of all ICOHP values of the Ce−T bonds around Ce2 for each model and comparison will automatically favor all models having at least one Ce−Ru bond simply because the ICOHP of this bond is always higher than that of a Ce−Ni bond at the same distance. This method will therefore make model B the most stable. However, the weakness of this method is the comparison of two different bonds (Ce−Ni and Ce−Ru).

In the second method, only energy differences between comparable bonds in different models are taken into account: For example, the short Ce−Ru bond of model B is compared with those of models D and E, whereas the short Ce−Ni of model C is compared with those of models D and E. The same also applied for the larger bonds. As a result, the overall ICOHP difference (ΔICOHP) between models D and B is −0.21 eV (−20.26 kJ mol^{-1}) in favor of B, while between D and E, ΔICOHP is −0.06 eV (−5.79 kJ mol^{-1}) in favor of E. On the other hand, ΔICOHP is about −0.13 eV (−12.54 kJ mol^{-1}) between C and D in favor of D, while between B and E, ΔICOHP is −0.04 eV (−3.86 kJ mol^{-1}) in favor of E. From this second method, model E is favored, which is just −3.86 kJ mol^{-1} better than model B. The weakness of this second method is that all bonds cannot be compared because some are replaced by different ones from model to model. However, in

dx.doi.org/10.1021/ic402414f | Inorg. Chem. 2014, 53, 2471−2480

Table 6. Bond Lengths and ICOHP Values of the Shortest Ce−T Bond (T = Ru or Ni)

alloy (structure)	model	cerium atom in the Ce−T bond	shortest Ce−Ru distance (pm)	shortest Ce−Ni distance (pm)	ICOHP Ce−Ru (eV)	ICOHP Ce−Ni (eV)
CeRuAl (CeRuAl structure)		Ce2	280.3		−1.88	
CeNiAl (CeRuAl structure)		Ce2		280.3		−0.95
CeNiAl ($CeRu_{0.5}Ni_{0.5}Al$ structure)	A	Ce2		268.2		−1.21
$CeRu_{0.5}Ni_{0.5}Al$	B	Ce2	268.2		−2.26	
		Ce2		294.8		−0.73
		Ce2		297.6		−0.67
$CeRu_{0.5}Ni_{0.5}Al$	C	Ce2		268.2		−1.25
		Ce2	294.8		−1.20	
		Ce2	297.6		−0.96	
$CeRu_{0.5}Ni_{0.5}Al$	D	Ce2a	268.2		−2.23	
		Ce2b		268.2		−1.33
		Ce2a	294.8		−1.18	
		Ce2b		294.8		−0.69
		Ce2a		297.6		−0.53
		Ce2b	297.6		−1.03	
$CeRu_{0.5}Ni_{0.5}Al$	E	Ce2a	268.2		−2.26	
		Ce2b		268.2		−1.27
		Ce2a		294.8		−0.74
		Ce2b	294.8		−1.21	
		Ce2a	297.6		−0.87	
		Ce2b		297.6		−0.70

both methods, it is obvious that the presence of a short Ce−Ru bond is necessary for the stability of the $CeRu_{1-x}Ni_xAl$ (x = 0.5) solid solution. This finding is further strengthened by the fact that the ICOHP value of the short Ce−Ni bond increases when a short Ce−Ru bond is present (see Table 6).

We can therefore conclude that the presence of at least one short Ce−Ru bond is necessary for the building of any composition in this solid solution. In fact, during the substitution of nickel for ruthenium, the solid solution is only stable when at least one short Ce−Ru bond exists. This means that we can have a maximum of 7 out of 8 ruthenium positions that may be substituted by nickel (x = 0.875). The last ruthenium position has to be involved in a short Ce−Ru bond. This could explain why there is no solid solution with orthorhombic crystal structure beyond x = 0.85 because further substitution of nickel for ruthenium would lead exclusively to short Ce−Ni bonds, a strong destabilizing factor.

CONCLUSIONS

In this paper, we describe the synthesis and characterization of the solid solution $CeRu_{1-x}Ni_xAl$ for x = 0.1−0.95. For x = 0.1−0.85, the compound crystallizes in the orthorhombic LaNiAl-type structure, while for x = 0.9−1, the hexagonal ZrNiAl-type structure is found. For the orthorhombic members, an anomaly in the lattice parameters has been found, manifesting in a kink at x = 0.4. A comparison with the $LaRu_{1-x}Ni_xAl$ series, exhibiting no anomaly, has led to the conclusion that the effects seen in the cerium series have to be attributed to an electronic phenomenon rather than an issue of the size of the transition-metal atoms. Furthermore, all compounds have very short Ce−Ru distances, which also show the anomaly, while other interatomic distances change linearly as expected. The investigations of the magnetic properties indicate valence fluctuations due to the two possible oxidation states of the cerium cations. The magnetic susceptibilities have been fitted using the Sales and Wohlleben model for ICF, and the cerium valence has been calculated from the fitted parameters. The cerium valence for the individual members of the series drops with increasing nickel content, and the intermediate valence state has been verified by XANES investigations for $CeRu_{0.5}Ni_{0.5}Al$. For x = 0.4, a jump in the cerium valence can be found, which is consistent with the anomaly observed in the lattice parameters and interatomic distances. This has to be attributed to the change in the VEC and the short Ce−Ru bonds found in the structure. Theoretical calculations have shown that the stability range of the series is determined by the amount of ruthenium present in the structure. The short Ce−Ru bonds are the reason for the compounds to be stabilized over such a long existence range if a minimal amount of $^1/_8$Ru (x = 0.875) is present. This is consistent with the experimentally found end member $CeRu_{0.15}Ni_{0.85}Al$ in this structure type.

EXPERIMENTAL SECTION

Synthesis. The members of the $CeRu_{1-x}Ni_xAl$ series were synthesized from the elements, using cerium ingots (Sigma Aldrich), nickel wire (Alfa Aesar), ruthenium powder (Allgussa), and aluminum turnings (Koch Chemicals) with stated purities of 99.9% or higher. Pieces of the cerium ingot were arc-melted under an argon pressure of 800 mbar in a water-cooled copper hearth first. The ruthenium powder was pressed into pellets with a diameter of 6 mm. All starting materials were weighed in a stochiometry of 36:(32 − X):X:32 (Ce/Ru/Ni/Al) with the respective ratios of Ni/Ru and then arc-melted under argon at 800 mbar. The obtained button was remelted several times to increase the homogeneity. All samples were annealed in a second step to ensure that phase-pure products were used for subsequent measurements because the buttons obtained from the arc-melting step were not always phase-pure. For annealing, pieces of the arc-melted button were sealed in quartz ampules and tempered at 850 °C for 8 days. The furnace was cooled to room temperature within 24 h.

Powder XRD. The polycrystalline samples were characterized by Guinier patterns (imaging plate detector, Fujifilm BAS-1800 scanner) with Cu Kα_1 radiation using α-quartz (a = 491.30 pm; c = 540.46 pm) as an internal standard. Correct indexing of the diffraction lines was ensured through intensity calculations. The lattice parameters were obtained through least-squares fits.[23]

dx.doi.org/10.1021/ic402414f | Inorg. Chem. 2014, 53, 2471−2480

Single-Crystal X-ray Data. Small single crystals were selected from the as-cast arc-melted samples and first investigated via Laue photographs on a Buerger camera (white molybdenum radiation), equipped with the same Fujifilm BAS-1800 imaging-plate technique as the powder XRD cameras, in order to check the quality of the crystal for intensity data collection. Intensity data of the $CeRu_{1-x}Ni_xAl$ crystals were collected at room temperature using a Stoe IPDS II diffractometer (graphite-monochromatized Mo Ka radiation; oscillation mode).

EDX Data. Semiquantitative EDX analyses on all bulk samples were carried out on a Leica 420i scanning electron microscope. The polycrystalline pieces from the arc-melted buttons or from the tempered pellets were embedded in a methyl methacrylate matrix and polished with diamond and SiO_2 emulsions of different particle sizes. The experimentally observed compositions were close to the weighed ones, and phase-pure samples with respect to the limitations of the instrument were observed after annealing. No impurity elements heavier than sodium (detection limit of the instrument) were observed. Compositions for x = 0.1−0.9 are given in Table S8 in the Supporting Information.

Magnetization. Polycrystalline pieces of the annealed pellets were packed in kapton foil and attached to the sample holder rod of a vibrating sample magnetometer unit for measuring the magnetization $M(T,H)$ in a Quantum Design physical property measurement system. The samples were investigated in the temperature range of 2−350 K and with magnetic flux densities of 10 kOe.

XANES. XAS spectra at the Ce L_{III}-edge (5723 eV) were collected at BM01B (SNBL) at ESRF, Grenoble, France. The measurements were performed in transmission mode using a Si(111) double-crystal monochromator. The second crystal of the monochromator was detuned by 60% in order to suppress higher harmonic radiation. Experimental data were recorded in $Ce_2(CO_3)_3$ and CeO_2 as reference compounds with cerium in trivalent and tetravalent states, respectively. In order to optimize the edge jump, the powdered samples were homogeneously mixed with small amounts of cellulose and pressed into pellets. Measurements were performed at ambient conditions. The samples were first ground in an agate mortar with cyclohexane to avoid oxidation, then homogeneously mixed with small amounts of cellulose powder (Sigma-Aldrich) in order to optimize the edge jump, and pressed into pellets. The *Athena* software was used for processing and fitting of the data.[31]

Theoretical Methodology. The quantum-chemical calculations were carried out using the tight-binding, linear muffin-tin orbitals with the atomic sphere approximation (TB-LMTO-ASA)[24,25] as implemented in the *TB-LMTO 4.7* program.[26] Exchange and correlation were treated with the LDA functional as parametrized by von Barth and Hedin.[27] The k-mesh for all used structures was 15 × 29 × 7, which leads to either 480 k-points in the irreducible Brillouin zone (IBZ) for CeTAl (T = Ru or Ni, with the experimental CeRuAl structure) and model A or 795 k-points in the IBZ for models B−G. For details about these models, see the Supporting Information (Tables S6 and S7). The radii of the automatically generated Wigner−Seitz cells for cerium, ruthenium, nickel, and aluminum were 1.72−1.83, 1.51−1.54, 1.45−1.47, and 1.52−1.62 Å, respectively, for CeTAl (with the experimental parameters of CeRuAl) and 1.62−1.83, 1.45−1.53, 1.38−1.50, and 1.47−1.58 Å, respectively, for models A−G. Because there is no close package of the atoms, empty spheres were needed for the LMTO calculations. Bonding analysis was done by calculation of the DOS and the crystal orbital Hamilton population (COHP)[28] and its integrals (ICOHP). The ICOHP can be seen as a semiquantitative bonding energy that measures the covalent contribution in solids. Because −COHP values are plotted, negative −COHP are antibonding states, positive ones are bonding states, and nonbonding states have a −COHP value of zero. The Fermi level was set to 0 eV as a reference.

■ ASSOCIATED CONTENT

Supporting Information

X-ray crystallographic data in CIF format, additional single-crystal data (Tables S1−S4) as well as all theoretical models (Tables S6 and S7) and additional DOS curves (Figure S1), EDX analysis of the samples (Table S8), and fitting of the XANES data (Figure S2). This material is available free of charge via the Internet at http://pubs.acs.org.

■ AUTHOR INFORMATION

Corresponding Author

*E-mail: ocjanka@uni-muenster.de. Tel: +49 (0)251 83-36074. Fax: +49 (0)251 83-36002.

Author Contributions

The manuscript was written through contributions of all authors. All authors have given approval to the final version of the manuscript.

Notes

The authors declare no competing financial interest.

■ ACKNOWLEDGMENTS

O.N. is indebted to the NRW Forschungsschule (Molecules and Materials—A common Design Principle) for a Ph.D. stipend. B.P.T.F. thanks Deutsche Forschungsgemeinschaft for financial support through the Heisenberg fellowship. O.J. is indebted to the German Academic Exchange Service (DAAD) for a scientist return scholarship.

■ REFERENCES

(1) Szytuła, A.; Leciejewicz, J. *Handbook of Crystal Structures and Magnetic Properties of Rare Earth Intermetallics*; CRC Press: Boca Raton, FL, 1994.

(2) Gribanov, A. V.; Tursina, A. I.; Grytsiv, A. V.; Murashova, E. V.; Bukhan'ko, N. G.; Rogl, P.; Seropegin, Y. D.; Giester, G. *J. Alloys Compd.* **2008**, *454*, 164−167.

(3) Hermes, W.; Matar, S. F.; Pöttgen, R. *Z. Naturforsch.* **2009**, *64b*, 901−908.

(4) Bandyopadhyay, B.; Ghoshray, K.; Ghoshray, A.; Chatterjee, N. *Phys. Rev. B* **1988**, *38*, 8455−8458.

(5) Menon, L.; Agarwal, A.; Malik, S. K. *Physica B* **1997**, *230−232*, 201−203.

(6) Gout, D.; Benbow, E.; Gourdon, O.; Miller, G. J. *J. Solid State Chem.* **2003**, *176*, 538−548.

(7) Janka, O.; Baumbach, R. E.; Ronning, F.; Thompson, J. D.; Bauer, E. D.; Kauzlarich, S. M. *Z. Anorg. Allg. Chem.* **2012**, *638*, 1996−2000.

(8) Fickenscher, T.; Hoffmann, R.-D.; Kraft, R.; Pöttgen, R. *Z. Anorg. Allg. Chem.* **2002**, *628*, 667−672.

(9) Riecken, J. F.; Hermes, W.; Chevalier, B.; Hoffmann, R.-D.; Schappacher, F. M.; Pöttgen, R. *Z. Anorg. Allg. Chem.* **2007**, *633*, 1094−1099.

(10) Mishra, T.; Hoffmann, R. D.; Schwickert, C.; Pöttgen, R. *Z. Naturforsch.* **2011**, *66b*, 771−776.

(11) Hirst, L. L. *Phys. Kondens. Mater.* **1970**, *11*, 255−278.

(12) Sales, B. C.; Wohlleben, D. K. *Phys. Rev. Lett.* **1975**, *35*, 1240−1244.

(13) Niehaus, O.; Abdala, P. M.; Riecken, J. F.; Winter, F.; Chevalier, B.; Pöttgen, R. *Z. Naturforsch.* **2013**, *68b*, 960−970.

(14) Kotani, A.; Kvashnina, K. O.; Glatzel, P.; Parlebas, J. C.; Schmerber, G. *Phys. Rev. Lett.* **2012**, *108*, 036403.

(15) Chaboy, J.; Marcelli, A.; Bozukov, L.; Baudelet, F.; Dartyge, E.; Fontaine, A.; Pizzini, S. *Phys. Rev. B* **1995**, *51*, 9005−9014.

(16) Isnard, O.; Miraglia, S.; Buschow, K. H. J. *Physica B* **1997**, *239*, 365−369.

(17) Chondroudi, M.; Peter, S. C.; Malliakas, C. D.; Balasubramanian, M.; Li, Q. A.; Kanatzidis, M. G. *Inorg. Chem.* **2011**, *50*, 1184−1193.
(18) Paul-Boncour, V.; Joubert, J. M.; Latroche, M.; Percheron-Guégan, A. *J. Alloys Compd.* **2002**, *330*−*332*, 246−249.
(19) Shablinskaya, K.; Murashova, E.; Tursina, A.; Kurenbaeva, Z.; Yaroslavtsev, A.; Seropegin, Y. *Intermetallics* **2012**, *23*, 106−110.
(20) Tsvyashchenko, A. V.; Fomicheva, L. N.; Sorokin, A. A.; Ryasny, G. K.; Komissarova, B. A.; Shpinkova, L. G.; Klementiev, K. V.; Kuznetsov, A. V.; Menushenkov, A. P.; Trofimov, V. N.; Primenko, A. E.; Cortes, R. *Phys. Rev. B* **2002**, *65*, 174513.
(21) Yaroslavtsev, A.; Menushenkov, A.; Chernikov, R.; Clementyev, E.; Lazukov, V.; Zubavichus, Y.; Veligzhanin, A.; Efremova, N.; Gribanov, A.; Kuchin, A. *Z. Kristallogr.* **2010**, *225*.
(22) Niewa, R.; Hu, Z.; Grazioli, C.; Rößler, U.; Golden, M. S.; Knupfer, M.; Fink, J.; Giefers, H.; Wortmann, G.; de Groot, F. M. F.; DiSalvo, F. J. *J. Alloys Compd.* **2002**, *346*, 129−133.
(23) Yvon, K.; Jeitschko, W.; Parthé, E. *J. Appl. Crystallogr.* **1977**, *10*, 73−74.
(24) Andersen, O. K.; Skriver, H.; Nohl, H.; Johansson, B. *Pure Appl. Chem.* **1980**, *52*, 93−118.
(25) Andersen, O. K.; Jepsen, O. *Phys. Rev. Lett.* **1984**, *53*, 2571−2574.
(26) Andersen, O. K.; Tank, R. W.; Jepsen, O. *TB-LMTO-ASA*, version 4.7; Max-Planck-Institut für Festkörperforschung: Stuttgart, Germany, 1998.
(27) von Barth, U.; Hedin, L. *J. Phys. C: Solid State Phys.* **1972**, *5*, 1629.
(28) Dronskowski, R.; Bloechl, P. E. *J. Phys. Chem.* **1993**, *97*, 8617−8624.
(29) Sheldrick, G. M. *Acta Crystallogr.* **2008**, *A64*, 112−122.
(30) Hahn, T., Wilson, A. J. C., Eds. *International Tables for Crystallography*; Kluwer Academic Publishers: Dordrecht, The Netherlands, 1992; Vol. *C*.
(31) Ravel, B.; Newville, M. J. *Synchrotron Rad.* **2005**, *12*, 537−541.